A Reformulation of the Pseudo2D Battery Model Coupling Large Electrochemical-Mechanical Deformations at Particle and Electrode Levels

Weijie Mai,* **Andrew Colclasure,** **and Kandler Smith*,z**

National Renewable Energy Laboratory, Golden, Colorado 80401, USA

The Pseudo2D electrochemical reaction/transport battery model is consistently reformulated based on the finite strain theory to incorporate the coupled effects of large electrochemical-mechanical deformations at both particle and electrode levels. The active material volume change due to lithium insertion/extraction causes the electrode deformation and porosity variation. The porosity variation affects the mechanical properties of each component of the cell as well as the transport processes. In turn, the electrode deformation also affects porosity variation and the electrochemical processes (transport and equilibrium potential). Variables such as particle size and specific surface area are also simultaneous updated based on the approximated electrode deformation and porosity distributions. The model is applied to simulate the performance of a cell composed of Si anode and NMC532 cathode to study the effect of active material volume change on the cell performances. The simulation results show that during the charging process the porosity of each cell component experiences significant reduction due to the large expansion of Si particles. Also, a notable hydrostatic stress develops within the cell, which introduces an overpotential in addition to that caused by porosity reduction. The model is also employed to study the effects of charging rate, initial anode porosity, cell loading and fixture condition.
 [DOI: 10.1149/2.0101908jes]

Manuscript submitted January 31, 2019; revised manuscript received April 2, 2019. Published April 22, 2019.

Lithium ion battery (LIB) has become the primary energy storage option for electric vehicles (EVs) due to their relatively high energy and power densities.[1] However, in order to compete with conventional vehicles that use fossil energy, lithium ion battery should be further improved in terms of energy and power densities, safety, cost, etc.[2] One of the strategies to increase the energy density is to use electrode materials with high capacty, such as Li-alloy materials.[3] However, concomitant with the high capacity of these materials is their high volume change during lithium insertion, which not only causes fracture of active particles but also leads to electrode and cell deformations that could deteriorate cell performances. It is therefore necessary to investigate the effects of both particle-level and electrode-level deformations for better design of electrode using high capacity materials.

There are many models in literature that can predict the deformation and stress generation within a single particle during Li insertion/extraction.[4–6] Most of these models assume infinitesimal deformation and thus are not suitable for modeling the volume change of active material with high capacity, which can undergo more than 100% expansion during Li insertion. Although some recent models have been developed based on the finite strain theory to approximate the large active material volume change,[7,8] its effect on electrode deformation and the performance of the entire cell cannot be investigated using these single particle models. On the other hand, most of the electrode level models that approximate the electrochemical process during battery cycling have assumed constant volumes for both active particles and the entire cell.[9,10] A few models, while still assuming constant particle and electrode dimensions, incorporated the effect of particle volume change by relating the electrode porosity variation with lithium intercalation.[11,12] More recently, Gomadam et al.[13] took a step further and developed a model that can approximate both the dimensional change and the porosity variation of the electrode due to lithium intercalation by introducing a swelling coefficient. Using similar governing equations for porosity variation, Garrick et al.[14,15] applied the porous rock mechanics to account for stress built up in electrodes. However, these models still ignored the large deformation at particle level, which should be coupled with electrode deformation and porosity variation. Solid diffusion and lithium insertion/extraction on particle surface are also affected by particle deformation, the effect of which should not be ignored for high-capacity materials.

The objective of this work is to develop a one-dimensional model of lithium ion battery that consistently couples electrochemistry, porosity variation and deformations at both the particle and electrode levels. In this model, particle and electrode domains are described with respective 1D spherical and 1D Cartesian coordinate systems (hence the name "Pseudo2D" or P2D model) following the work of Newman et al.[9,10] The finite strain theory is employed to describe deformations of individual particles and the porous cell components. To account for the effect of large electrochemical-mechanical deformations, both governing equations for porosity variation and electrochemistry are reformulated in the reference (undeformed) geometry, thus allowing approximation of field distributions on a fixed problem domain. Therefore, this model provides an efficient way to investigate the coupled effect of particle volume change, porosity variation and external cell constraint on the overall performances of a cell composed of high capacity electrode. While this model is general and can be applied to other electrode combinations, a cell composed of silicon negative electrode and NMC532 positive electrode is chosen for investigation in this work. This model enables us to investigate the effects of component porosities, charge/discharge rate, loading and fixture condition on the capacity and energy density of the cell, which should prove useful in the design of cell composed of high capacity electrode.

Problem Formulation

Electrode deformation.—In this work, the finite strain theory is employed to approximate electrode deformation and stress due to active material volume change and external constraint. The electrode deformation can be described by the deformation gradient tensor $\mathbf{F}$

$$\mathbf{F} = \mathbf{I} + \nabla \mathbf{u}, \quad [1]$$

where $\mathbf{I}$ is the identity tensor and $\mathbf{u}$ is the displacement vector. $\mathbf{F}$ can be multiplicatively decomposed into two terms such that $\mathbf{F} = \mathbf{F}_e\mathbf{F}_c$, where $\mathbf{F}_e$ and $\mathbf{F}_c$ correspond to elastic deformation gradient tensor and the inelastic deformation gradient tensor induced by Li insertion/extraction, respectively. Assuming isotropic volume expansion, $\mathbf{F}_c$ can be expressed as

$$\mathbf{F}_c = \left(1 + \frac{\Omega_e}{3}\Delta C_{s,avg}\right)\mathbf{I}. \quad [2]$$

*Electrochemical Society Member.
zE-mail: Kandler.Smith@nrel.gov

In the above equation, Ω_e is the partial molar volume of Li in the electrode. $\Delta C_{s,avg} = C_{s,avg} - C_{s,avg,0}$ is the change of the average nominal solid concentration $C_{s,avg}$. The definition of nominal solid concentration will be given in Pseudo2D model with large deformation section.

The second Piola-Kirchhoff stress tensor within the electrode can be defined as

$$\mathbf{S} = J_c \mathbf{F}_c^{-T}(\mathbf{C} : \epsilon_e)\mathbf{F}_c^{-1}, \quad [3]$$

where $J_c = \det(\mathbf{F}_c)$ is the volume change induced by lithium insertion/extraction, $\mathbf{C}$ is the stiffness tensor and $\epsilon_e = \frac{1}{2}(\mathbf{F}_e^T\mathbf{F}_e - \mathbf{I})$ is the elastic strain tensor. Assuming quasi-steady stress distribution, the governing equation for the displacement vector $\mathbf{u}$ can be expressed as

$$\nabla \cdot (\mathbf{FS})^T = 0. \quad [4]$$

After approximating the distribution of $\mathbf{u}$ using Equation 4 with proper boundary conditions, the distribution of $\mathbf{S}$ can be recovered using Equation 3, which can then be transformed to the Cauchy stress $\boldsymbol{\sigma}$ using the following relation

$$\boldsymbol{\sigma} = J^{-1}\mathbf{FSF}^T, \quad [5]$$

where J is the total Jacobian of deformation. Assuming that a material volume dV_0 in the undeformed electrode expands to dV due to Li insertion/extraction, the total Jacobian can be defined as

$$J = \det(\mathbf{F}) = \frac{dV}{dV_0}. \quad [6]$$

As the porous electrodes are relatively thin, their in-plane movement will be significantly constrained by the current collectors which have much larger elastic modulus.[16,17] Therefore, in this work only the deformation in the thickness direction is considered, which simplifies the problem to one-dimensional. However, it should be pointed out that while the in-plane displacement is considered negligible, the in-plane stress is significant and dominates the hydrostatic stress within the cell. The effect of hydrostatic stress on the OCP of Si is incorporated into the model and its significance will be discussed in following sections.

Porosity variation.—As a result of lithium insertion/extraction, the active material storing Li either expands or contracts, which will alter the porosity and size of electrode. It has been proposed that the porosity and dimension variations of porous electrode can be approximated using the following equation[13]

$$\frac{\partial \varepsilon_s}{\partial t} + \nabla \cdot (\varepsilon_s \mathbf{v}) = -\frac{s\Omega_e}{nF} j, \quad [7]$$

where ε_s is the volume fraction of the solid phase, $s = 1$ is the stoichiometric coefficient, $\mathbf{v}$ is the local electrode velocity vector and j is the volumetric reaction current source. The physical meaning of the above equation is that the volume change of solid phase induced by lithium insertion/extraction will cause either porosity variation or dimensional change of the electrode.[14,15] To approximate the solution of Equation 7, it has to be coupled with solid mechanics approximation, which will provide the distribution of $\mathbf{v}$. As the local electrode velocity is associated with the deformed electrode geometry, the problem domain will have to be frequently updated unless infinitesimal deformation is assumed. Alternatively, the governing equation for porosity variation can be formulated in the undeformed geometry, such that it can be approximated on a fixed geometry

$$\frac{\partial(\varepsilon_s J)}{\partial t} = -\frac{s\Omega_e}{nF} jJ. \quad [8]$$

In the above equation, J is the Jacobian of deformation defined in Electrode deformation section. Note that by formulating the governing equation in the undeformed geometry, the convection term due to electrode deformation is eliminated. Instead, the information of electrode deformation is now represented by the deformation Jacobian J. It should also be noted that ε_s approximated using Equation 8 is the solid volume fraction in the deformed geometry, while the nominal solid volume fraction evaluated based on undeformed geometry is $\varepsilon_s J$. Finally, in this work it is assumed that the partial molar volume of Li in the porous electrode equals to that in the active material,[18] i.e., all the active material volume change due to lithium insertion/extraction is translated to electrode dimensional change when the electrode is free of constraint.

In Equation 8, the effect of electrode deformation on porosity variation is incorporated by the Jacobian J. However, porosity variation should also influence electrode deformation by affecting the mechanical properties of the porous cell components. As experimental data is not available at present, in this work it is assumed that the elastic modulus and Poisson's ratio of each component are power functions of porosity ε_e,[19] such that

$$E = E_s(1 - \frac{\varepsilon_e}{\varepsilon_0})^n, \quad [9]$$

$$\nu = \nu_s + \frac{\varepsilon_e}{\varepsilon_1}(\nu_0 - \nu_s) \quad [10]$$

In the above equations, E_s and ν_s correspond to the elastic modulus and Poisson's ratio of a component when it is pore-free, i.e., $\varepsilon_e = 0$. $n = 2.23$ and $\varepsilon_0 = 0.652$ are empirical correlation parameters. $\nu_0 = 0.140$ and $\varepsilon_1 = 0.472$ are fitting parameters.

Pseudo2D model with large deformation.—The popular P2D model is formulated on a fixed geometry, the deformation of which has been ignored. To allow approximating fields on a fixed domain with effect of deformation incorporated, the governing equations of the P2D model have to be reformulated. Here we first manipulate the governing equation for Li concentration c_s in the active material. Assume that before deformation active material in an electrode is composed of spherical particles of identical radius $\mathbb{R}$, which after deformation becomes $\mathbb{r}(x)$. As the lithium insertion/extraction rate is nonuniform within electrodes, $\mathbb{r}$ becomes location-dependent after cell cycling. Assume that a point located at R in an undeformed particle is moved to r after deformation. Then the deformation of the particle can be completely characterized by the particle deformation gradient tensor $\mathbf{F}_p$, which is defined as

$$\mathbf{F}_p = \begin{bmatrix} \frac{\partial r}{\partial R} & 0 & 0 \\ 0 & \frac{r}{R} & 0 \\ 0 & 0 & \frac{r}{R} \end{bmatrix}. \quad [11]$$

In a more complete formulation, a large deformation formulation should be used to relate the deformation and concentration distribution within the particle, as was done in Refs. 7,8. In this work, the major focus is on coupling the particle-level and electrode-level deformations, without resolving stress variations within individual particles. Therefore, in this work it is assumed that the deformation in each particle is uniform, such that

$$\frac{\partial r}{\partial R} = \frac{r}{R} = \lambda. \quad [12]$$

In the above equation, λ is the principal stretch and is uniform within each particle. However, due to the nonuniform reaction rate in the thickness direction, λ and thus particle expansion/contraction is not uniform within the electrode. The volume change of the particle can be characterized by the particle deformation Jacobian J_p, which is defined as

$$J_p = \det(\mathbf{F}_p) = \left(\frac{\mathbb{r}}{\mathbb{R}}\right)^3 = \lambda^3. \quad [13]$$

As a coupled multiphysics process, the volume change of the particle is related to porosity variation and electrode deformation. Therefore, the volume change of a particle can be equivalently expressed as

$$J_p = \frac{dV_s}{dV_{s,0}} = \frac{\varepsilon_s}{\varepsilon_{s,0}} J, \quad [14]$$

where dV_s and $dV_{s,0}$ are the current and initial differential solid volumes of a material volume, respectively. Similarly, ε_s and $\varepsilon_{s,0}$ are the current and initial solid volume fractions of the material volume. Note

that Equation 14 couples the particle level deformation with the electrode level deformation by relating J_p with J and ε_s. After the information of the particle deformation is obtained, the governing equation for solid phase concentration distribution can be expressed as

$$\frac{\partial}{\partial t}(J_p c_s) = -\frac{1}{R^2}\nabla_L(R^2\mathbf{J}_L), \quad [15]$$

where $\mathbf{J}_L$ is the flux density of Li and the underscore L indicates that the term is evaluated in the material frame, i.e., the undeformed geometry. Note that $C_s = J_p c_s$ is the nominal concentration evaluated in the undeformed geometry while c_s is the real concentration in the current deformed geometry. While $\mathbf{J}_L$ can be complicated by stress-induced diffusion[4,6] and the concentration-dependent diffusivity,[20] in this first attempt we only consider diffusion induced by a concentration gradient with a constant diffusivity D_s^E in the deformed geometry, i.e.,

$$\mathbf{J}_L = -D_s^L \nabla_L c_s = -J_p \mathbf{F}_p^{-1} D_s^E \mathbf{F}_p^{-T} \nabla_L c_s. \quad [16]$$

D_s^L is the effective diffusivity in the undeformed geometry, which ensures that the flux passing an undeformed surface equals to that passing the corresponding deformed surface. The boundary conditions for Equation 16 are as follows

$$\begin{aligned} \mathbf{J}_L \cdot \mathbf{n} &= 0|_{R=0} \\ \mathbf{J}_L \cdot \mathbf{n} &= -\frac{s i_E}{nF} J_p^{\frac{2}{3}}|_{R=\mathbb{R}}. \end{aligned} \quad [17]$$

The second boundary condition is derived based on mass conservation. More specifically, the flux density at the surface of deformed particle in the deformed electrode can be expressed as $\mathbf{J}_E \cdot \mathbf{n} = -\frac{s i_E}{nF}|_{r=\mathbb{r}}$. To ensure mass conservation, the total flux evaluated in the deformed and undeformed particle surfaces should be the same, i.e., $|\mathbf{J}_E| \times 4\pi\mathbb{r}^2 = |\mathbf{J}_L| \times 4\pi\mathbb{R}^2$. Then using relation 13 the second boundary condition in 17 can be obtained. i_E is the reaction current density evaluated at the surface of the deformed particle based on the Butler-Volmer equation

$$\begin{aligned} i_E &= i_0\left[\exp\left(\frac{\alpha_a F\eta}{nF}\right) - \exp\left(\frac{-\alpha_c F\eta}{nF}\right)\right] \\ i_0 &= F(k_c)^{\alpha_a}(k_a)^{\alpha_c}(C_{s,\max} - C_s)^{\alpha_a}(C_s)^{\alpha_c}\left(\frac{c_l}{c_{l,\text{ref}}}\right)^{\alpha_a} \\ \eta &= \phi_s - \phi_l - E^{\text{eq}}(x) \end{aligned} \quad [18]$$

In the above equation, i_0 is the exchange current density, $\alpha_a = \alpha_c = 0.5$ are the symmetry factors, η is the overpotential and E_{eq} is the equilibrium potential, which is a function of the intercalation fraction ($x = C_s/C_{s,\max}$) at the particle surface. It should be noted that as the maximum solid concentration $C_{s,\max}$ is defined assuming negligible volume change during Li intercalation, evaluations of i_0 and intercalation fraction should use the nominal concentration C_s instead of the real concentration c_s. While Equation 18 is widely used in LIB modeling, additional treatment is required for Si anode of which the polarization curve shows significant hysteresis that could be attributed to the effect of stress.[21] To account for the hysteresis of the polarization curve of Si, its equilibrium potential is expressed as

$$E_{\text{Si}}^{\text{eq}} = E_{\text{Si}}^{\text{eq}}(x) + \frac{\Omega\sigma_h}{F}, \quad [19]$$

where $\sigma_h = \text{trace}(\boldsymbol{\sigma})/3$ is the electrode-level hydrostatic stress. Due to the small size of the Si particle studied in this work, the effect of diffusion induced stress (DIS) is not considered in this work but will be incorporated in the future.

The governing equations for electrolyte and electric potentials are similar to those in the classic P2D model but expressed in the undeformed geometry, such that

$$\nabla_L \cdot i_l = jJ, \quad [20]$$

$$\nabla_L \cdot i_s = -jJ. \quad [21]$$

The right-hand-sides of the above equations are the equivalent volumetric current source in the undeformed electrode, while $j = a i_E$ is the real volumetric current source in the deformed electrode. a is the specific surface area of the active material in the deformed electrode, which can be expressed as

$$a = \frac{3\varepsilon_s}{\mathbb{r}(x)} = \frac{3\varepsilon_s}{\mathbb{R}} J_p^{-\frac{1}{3}}(x). \quad [22]$$

The above equation shows that the proposed model is able to approxiamte the variation of specific surface area, which requires the simultaneous and consistent approximations of particle size and solid volume fraction variations. Such capability has not been reported in literature to the best knowledge of the authors.

As the electrode porosity varies due to Li insertion/extraction, the pore-filling electrolyte either flows in to occupy additional pore volume or flows out to make room for the expanded active material. Assuming that the electrolyte concentration c_l only varies in the thickness direction and that the electrolyte only flows in and out in the in-plane direction, the following governing equation for c_l is derived

$$(1-\varepsilon_s)J\frac{\partial c_e}{\partial t} = \nabla_L \cdot \left[D_l^L \nabla_L c_e - \frac{\mathbf{i}_e t_+}{F}\right] + \frac{j}{nF}J. \quad [23]$$

The above equation also ensures mass conservation and that the electrolyte is incompressible. To account for the effect of deformation on transport properties, the effective electrolyte diffusivity D_l^L, electrolyte conductivity κ_l^L and the solid conductivity κ_s^L are evaluated using expressions similar to Equation 16. The explicit forms of the governing equations are summarized in Table AI.

Table I. Values of the parameters used in the current model for all example problems unless stated otherwise.

Parameter	Cathode	Separator	Anode
$\mathbb{R}$ (μm)	1.8	N/A	0.1
D_s (m²/s)	Table BI	N/A	1e-16
κ_s (S/m)	100	N/A	100
i_0 (A/m²)	Table BI	N/A	1
Ω (m³/mol)	7.8e-7[22]	N/A	9.0e-6[23]
$C_{s,\max}$ (kmol/m³)	49.6	N/A	333.3
$\varepsilon_{e,0}$	0.35	0.4	0.5
L_0 (μm) @ 5 mAh/cm², N:P=1.2	96.4	20	26.9
Intercalation fraction x	(0.3,0.9)	N/A	(0.1,0.6)
E_s(GPa)	2.5	1	5
ν	0.3	0.3	0.3
Bruggeman factor b	2.2	2.5	2.2

Results and Discussion

In this section, the proposed model is employed to investigate the electrochemical and mechanical behaviors of a cell composed of a Si anode and a NMC532 cathode with a cross-sectional area of 14.1 cm². The Si particles are assumed to be amorphous. Using parameter values summarized in Table I, the simulated cell is determined to have a theoretical capacity of 70.5 mAh (5 mAh/cm²). To single out the effects of component porosity variation and the stress-dependent OCP of Si on cell performances, three cases are considered in this section. Case I is the base case that corresponds to the classic P2D Newman model, which assumes negligible particle-level and electrode-level deformations. Case II incorporates the effect of active material volume change on porosity variation and electrode deformation, while Case III further incorporates the effect of stress-dependent OCP of Si. The cell is charged at constant current to the cut-off voltage $V_{\text{cut}} = 4.0727$ V with the two ends of the cell assumed to be fixed.

Figure 1a shows the variation of cell voltage versus charge capacity normalized by the theoretical capacity (70.5 mAh) when the cell is charged at 0.02C. It can be seen that at such low C rate, the voltage responses of Case I and Case II are similar and they can be charged to the theoretical capacity even though the model predicts a notable porosity reduction in all components of Case II when it is charged to

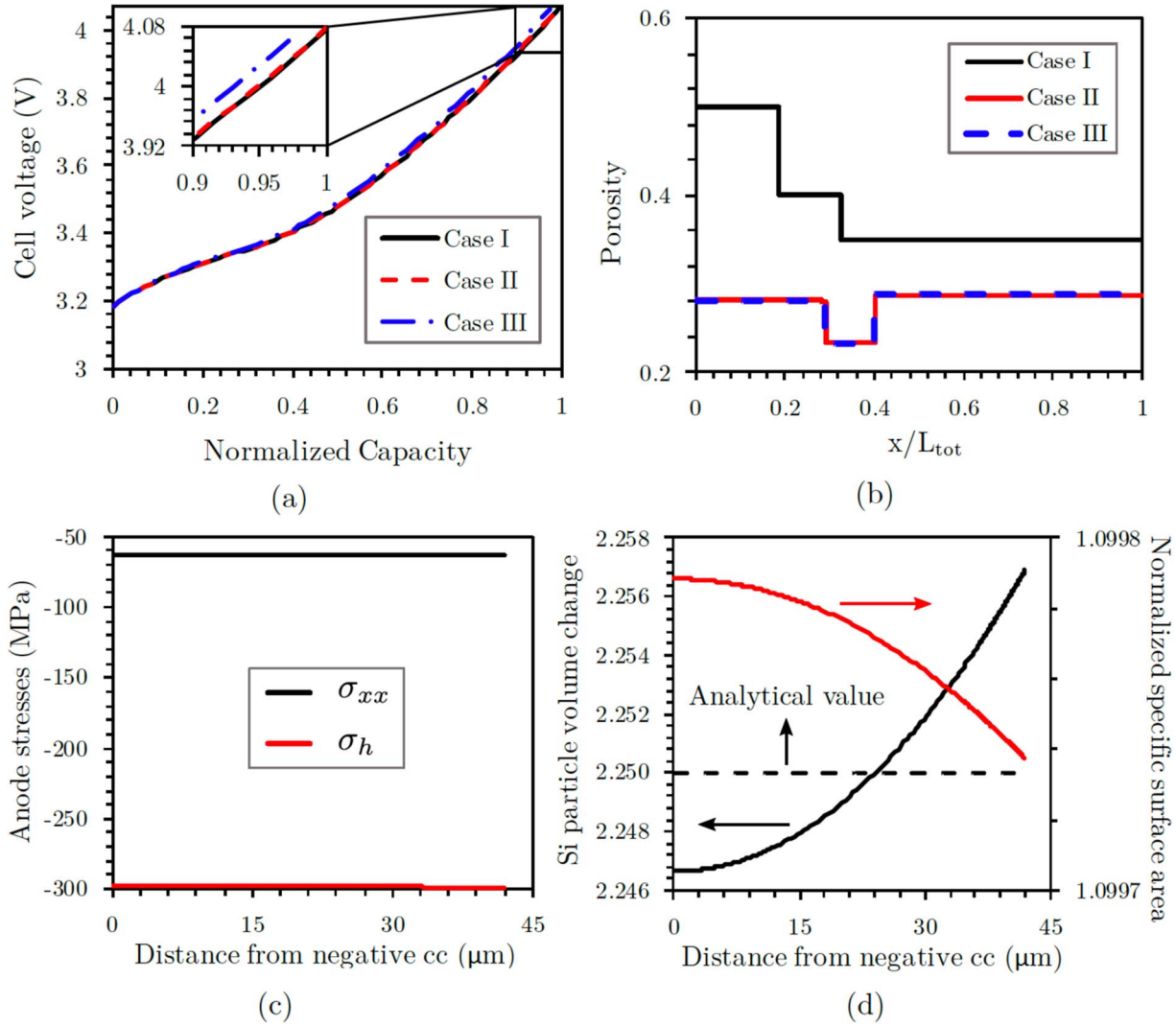

Figure 1. (a) Variation of cell voltage versus normalized charge capacity; (b) variation of porosity versus the normalized distance from the negative current collector (x/L_{tot}) when the cell is charged to 98.6% of the theoretical capacity; (c) and (d) show the distributions of σ_{xx} and σ_h, Si particle volume change (J_p) and particle specific surface area normalized by the initial specific surface area of the anode at end of charge for Case II, respectively. The charge rate is 0.02C.

98.6% of the theoretical capacity (maximum for Case III), as shown in Figure 1b. Note that the abscissa of Figure 1b is the distance from the negative current collector normalized by the total thickness of the cell (L_{tot} = 143.3 μm), which does not vary over time due to the fixed boundary condition. For Case I, the porosity of each component remains unchanged. In contrast, the porosities of anode, separator and cathode for Case II near the end of charge are reduced to 0.281 (reduced by 43.8%), 0.233 (reduced by 41.8%) and 0.287 (reduced by 18.0%), respectively. In spite of the significant porosity reduction, at a charge rate as low as 0.02C the ionic diffusion in electrolyte is still fast enough and thus it does not affect the voltage response of Case II. Figure 1b also shows the variation of the relative thickness of each component. For example, anode initially occupies approximately 18.8% of the total cell thickness, which is increased to about 29.0% near the end of charge due to Si expansion. Correspondingly separator and cathode are compressed.

The inset of Figure 1a shows that at the end of charge Case III has an additional overoptential of approximately 26.7 mV compared with Case I and Case II. This is due to the compressive hydrostatic stress within the anode developed during the charging process. Figure 1c shows the distributions of the out-of-plane stress σ_{xx} and the hydrostatic stress σ_h within the anode for Case II at the end of charge. As the cross-sectional area of the cell is assumed unchanged, σ_{xx} = −64 MPa is uniform over the cell thickness. σ_h is also approximately uniform within the anode in this case due to the uniform Si utilization at such low charging rate. The average σ_h within the anode is about −298 MPa, which corresponds to an overpotential of about 27.8 mV according to Equation 19. It should also be noted from Figure 1c that the magnitude of σ_h is notably larger than σ_{xx}, which indicates that the hydrostatic stress is dominated by the in-plane stress. While the negligible in-plane displacement assumption adopted in this work requires further validation, this simulation result sheds light on the potential significance of considering in-plane stress when studying electrode mechanical integrity, effect of stress on cell performances, etc.

Figure 1d shows the approximated variation of Si particle volume change (J_p) along the anode thickness at the end of 0.02C charge for Case II. It can be seen that while the Si particle near the separator is larger than that near the negative current collector ($x = 0$) due to the nonuniform Li insertion rate distribution, the magnitude of variation is actually very small due to the low charging rate. The average particle expansion is close to the analytical value ($J_p = 2.250$). Also shown in Figure 1d is the variation of the particle specific surface area of the anode (Equation 22) normalized by the initial specific surface area. It is predicted that the specific surface area is increased by about 10% at the end of charge, which may affect the power capability of the cell. Such predictive ability has not been reported in existing models, which

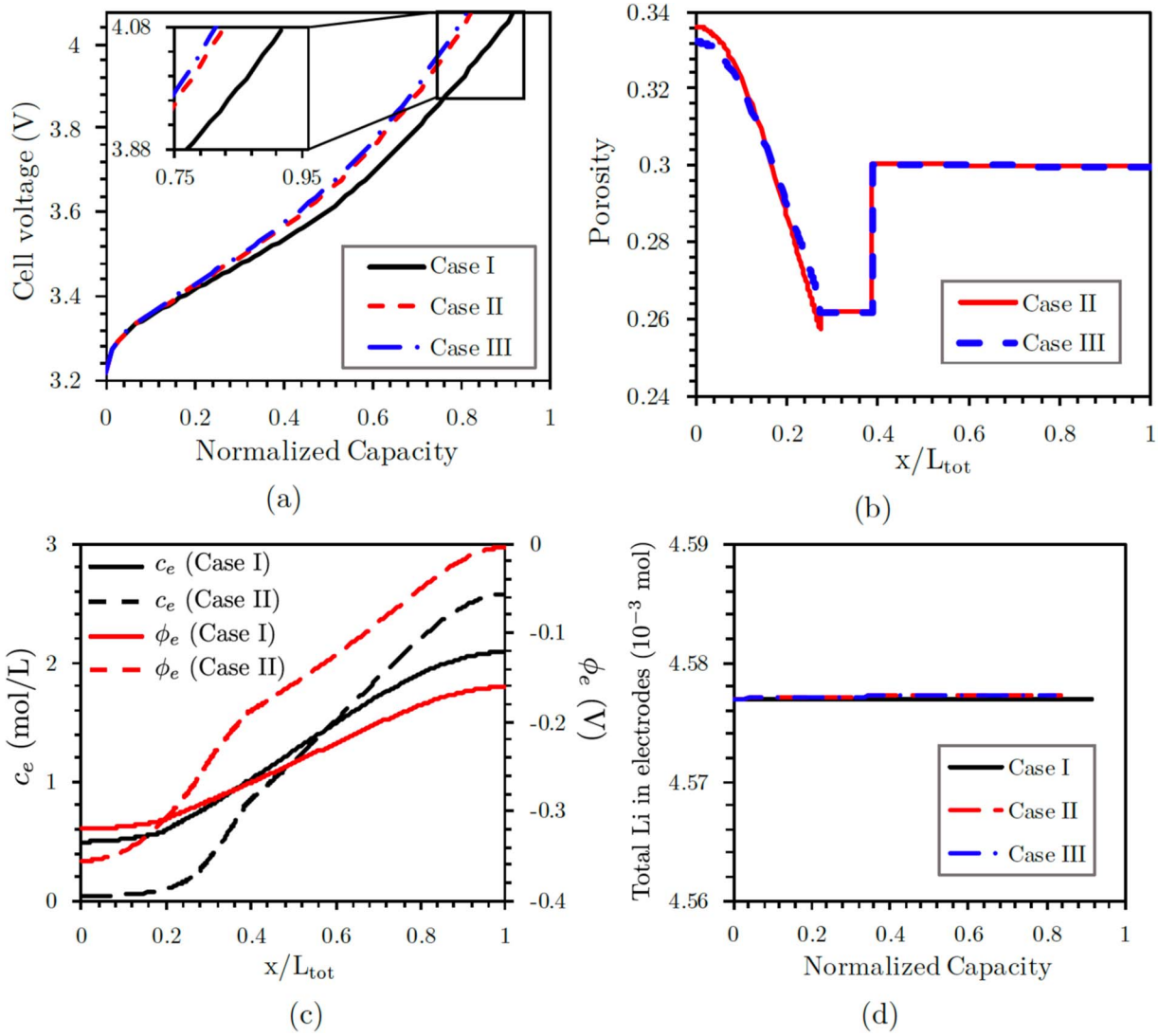

Figure 2. (a) Variation of cell voltage versus normalized charge capacity. (b) variation of porosity when the cell is charged to 81.9%; (c) variation of c_e and ϕ_e when the cell is charged to 83.3%; (d) variation of total amount of Li in electrodes. The charge rate is 1C.

requires the simultaneous and consistent determination of porosity and particle size variations.

Figure 2a shows the variation of cell voltage versus normalized charge capacity when the cell is charged at 1C. At the initial stage of charging, the voltage responses of all cases are similar, as the porosity reduction and compressive stress are still small in this stage. However, at the end of charge Case II has an additional overpotential of about 134.9 mV compared to Case I, which is due to the porosity reduction as shown in Figure 2b. Porosities in all components of Case I (not shown) do not change over time. In contrast, the porosities of anode, separator and cathode for Case II are reduced to about 0.290 (reduced by 42.0%), 0.262 (reduced by 34.5%) and 0.300 (reduced by 14.3%) respectively when the cell is charged to 81.9% of the theoretical capacity (maximum for Case III). In addition, as the lithium insertion rate in the anode is faster near the separator, the porosity is lower in this region due to larger Si particle expansion.

Figure 2c shows the variation of c_e and ϕ_e versus the normalized distance from the negative current collector for Case I and Case II when the cell is charged to 83.3% (maximum for Case II). Due to the porosity reduction, both the effective electrolyte diffusivity and conductivity are reduced for Case II, leading to larger differences of c_e and ϕ_e between the two ends of the cell. As shown in Figure 2c, the concentration and potential differences are increased by 59.1% and 120.9% when the effect of porosity reduction is incorporated, respectively. These are the direct reasons for the additional overpotential of Case II. As a result, while Case I can be charged to 91.7% of the theoretical capacity at 1C, Case II can only be charged to 83.3%. In addition, the electrolyte depletion in anode observed for Case II significantly reduce the the utilization of Si particles near the negative current collector. Figure 2d shows the variation of the total amount of Li stored in both electrodes, which should be conserved during the cycling process as side reactions (SEI formation, Li plating, etc.) are not considered in the current model. It is shown that the amount of Li is basically constant for Case II and Case III, with the maximum relative error being only 0.0066%. This simulation result together with those presented in Figure 1a and Figure 1d verify the formulation of the proposed model.

Distribution of intercalation fraction of active materials when the cell is charged to 81.9% at 1C is shown in Figure 3a. Compared with Case I, the ranges of intercalation fraction in both anode and cathode are significantly larger for Case II. This is due to the porosity reduction shown in Figure 2b which hinders the diffusion of lithium ions from cathode to anode. As a result, the active materials near the current collectors are less efficiently utilized, which implies nonuniform active material and electrode volume changes. Figure 3b shows the distribution of the electrode-level volume change (J) for Case II and

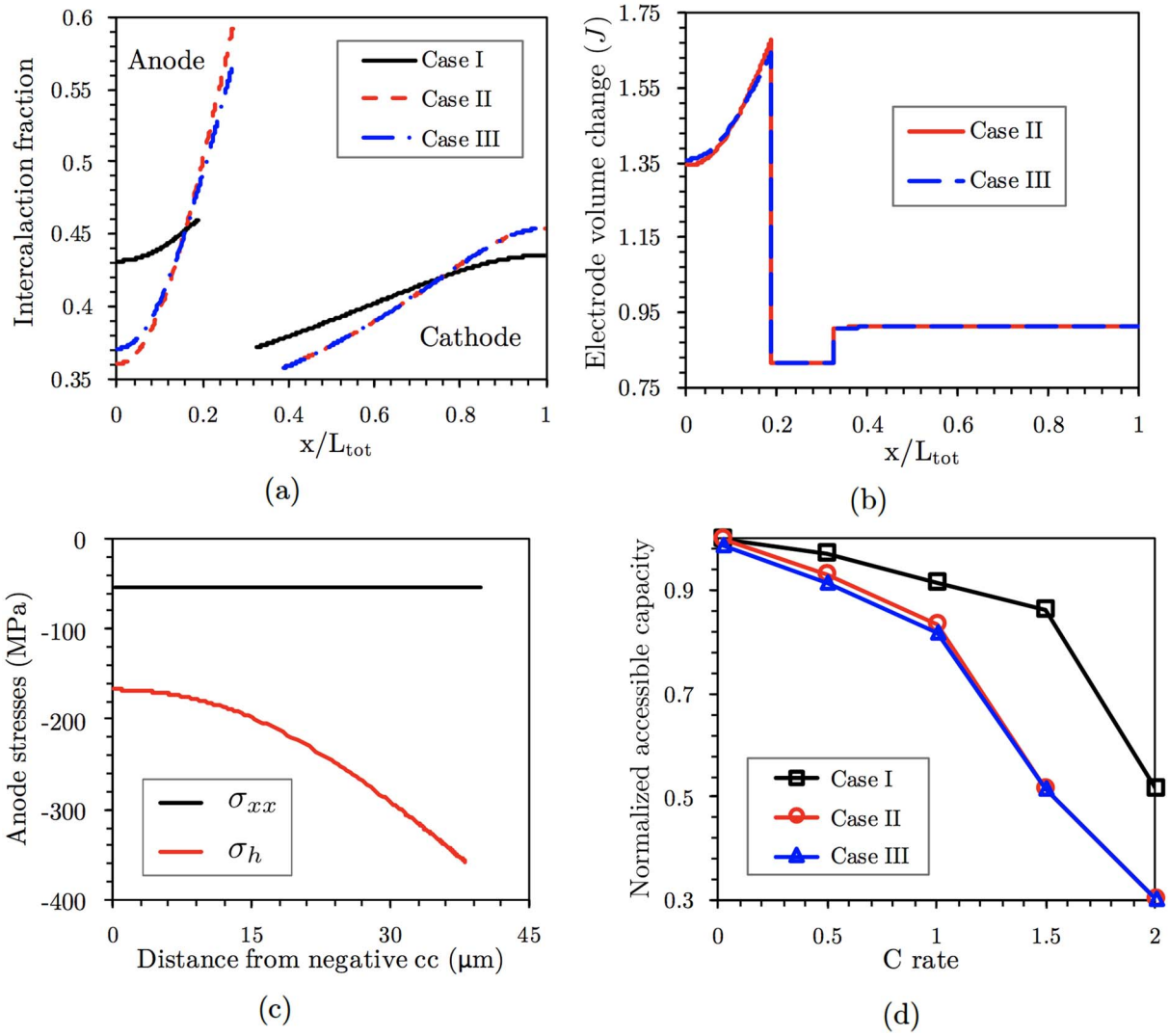

Figure 3. Variations of (a) intercalation fraction and (b) volume expansion of cell components versus the normalized distance from the negative current collector. (c) Distribution of anode stresses; (d) Variation of noramlized accessible capacity of the cell versus C rate.

III. It can be seen that the anode expansion varies from 1.34 near the negative current collector to 1.67 near the separator. The values of J in separator and cathode are 0.81 and 0.91 respectively and are relatively uniform. As a consequence of the nonuniform anode deformation, the distribution of σ_h in anode is also nonuniform as shown in Figure 3c. Due to the larger electrode expansion, a larger compressive hydrostatic stress is developed near the separator, while $\sigma_{xx} \approx -50$ MPa remains uniform within the anode. The nonuniform distribution of σ_h, which is coupled to the electrochemical process via Equation 19, alters the Li insertion rate distribution in anode. This coupling effect explains why the distributions of intercalation fraction and electrode volume change of Case III are slightly more uniform than Case II as shown in Figure 3a and Figure 3b.

As the porosity reduction mainly influences the ionic transport in the electrolyte, its effect is supposed to be more significant for high rate charging. Figure 3d presents the model prediction of the variation of normalized accessible capacity versus the C rate. At low C rate the major overpotential comes from the effect of hydrostatic stress on the equilibrium potential of Si. As the C rate increases, the effect of porosity reduction becomes dominant. When charged at 2C, the accessible charge capacity is overpredicted by 70% if the effect of active material volume change is neglected.

In addition to C rate, the effect of active material volume change is also affected by initial component porosities and loading of the cell. Figure 4a shows the voltage response of a cell with fixed loading (5 mAh/cm^2) and various initial anode porosity ($\varepsilon^a_{e,0}$) which is charged at 1C (Case III). It can be seen that the accessible capacity is generally decreasing with the decrease of $\varepsilon^a_{e,0}$. When $\varepsilon^a_{e,0}$ is below 0.45, the accessible capacity declines rapidly and the cell can only be charged to 45.8% when $\varepsilon^a_{e,0} = 0.35$. Figure 4b compares the variations of cell volumetric energy density versus $\varepsilon^a_{e,0}$ for Case I and Case III (thicknesses of current collectors are assumed to be 10 μm). As the relative contributions of porosity reduction and stress on cell performance has already been illustrated in previous examples, from now on only the predictions of Case I and Case III will be compared.

Intuitively, the energy density should first increase then decrease with the increase of $\varepsilon^a_{e,0}$ due to the higher mass transportation limitation at lower $\varepsilon^a_{e,0}$ and the larger cell volume at higher $\varepsilon^a_{e,0}$. Figure 4b shows that the cell energy density of Case I is monotonically decreasing with the increase of $\varepsilon^a_{e,0}$. This implies that when active material volume change is negligible, the ionic transportation in electrolyte is not limiting at 1C within the range of $\varepsilon^a_{e,0}$ investigated. Therefore, lower $\varepsilon^a_{e,0}$ can be used to obtain a higher energy density. Case III predicts a lower cell energy density at each $\varepsilon^a_{e,0}$ due to the additional overpotential associated with active material volume change. The difference between predictions is more notable at lower $\varepsilon^a_{e,0}$, where the pores in anode are almost completely closed at the end of charge and thus strongly

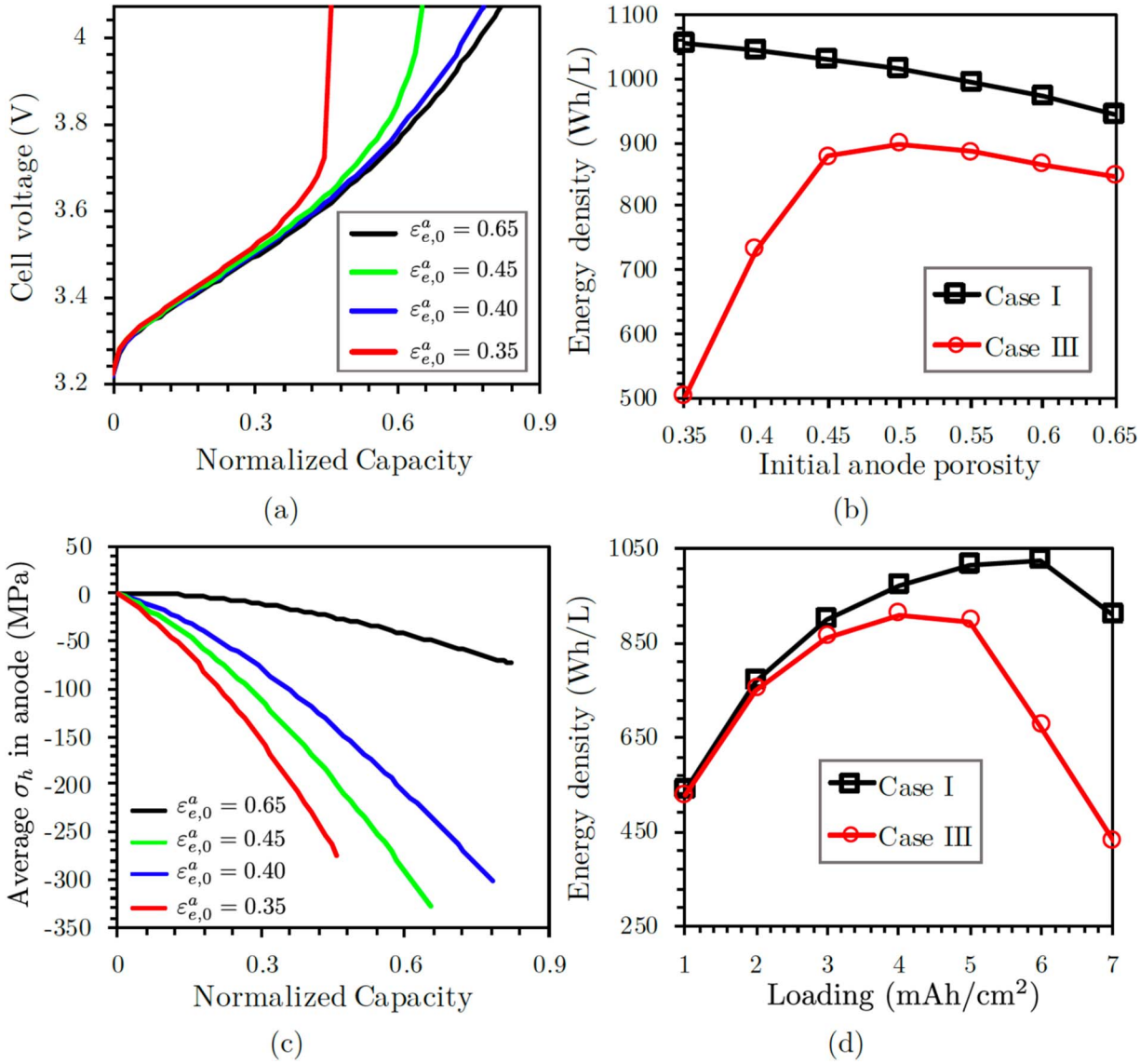

Figure 4. Variations of (a) cell voltage, (b) volumetric energy density and (c) average hydrostatic stress of anode for a cell with loading of 5 mAh/cm^2 and various initial anode porosity ($\varepsilon^a_{e,0}$). (d) Variation of volumetric energy density versus loading for a cell with $\varepsilon^a_{e,0} = 0.5$. All cells are charged at 1C. Both current collectors are assumed to have a thickness of 10 μm.

increase the concentration/ohmic overpotentials. For $\varepsilon^a_{e,0} = 0.35$, Case I overpredicts the energy density by 52%.

The model also predicts that the maximum energy density of the cell is 896.9 Wh/L which is achieved when $\varepsilon^a_{e,0} = 0.5$. However, it should be pointed out that the predicted optimal $\varepsilon^a_{e,0}$ is based on the modeled porosity instead of the recipe porosity, which does not consider the porosity reduction due to SEI formation. The effect of SEI on porosity reduction is especially significant for Si anode due to the small particle size (around 100 nm). Therefore, the optimal recipe anode porosity should be higher than that predicted in this example, such that after SEI formation the anode porosity is about 0.5.

Electrode porosity also affects the stress evolution within the cell by influencing its mechanical properties according to Equations 9 and 10. In this work, we are mainly interested in the stress within the Si anode, which is more prone to mechanical degradation. Figure 4c shows the evolution of the average hydrostatic stress of anode with various $\varepsilon^a_{e,0}$. When charged to the same capacity, the anode with lower initial anode porosity has a higher average hydrostatic stress due to the higher elastic modulus. Also note that for each $\varepsilon^a_{e,0}$ the gradient of average hydrostatic stress is decreasing as the charge capacity increases due to the gradual stiffening of the anode during the charging process.

Finally, Figure 4d demonstrates the variation of cell energy density versus cell loading for Case I and Case III ($\varepsilon^a_{e,0} = 0.5$). For fixed $\varepsilon^a_{e,0}$, the cell thickness is increasing with loading. When the loading is low (1 mAh/cm^2), the cell is relatively thin and thus porosity reduction due to active material volume change does not significantly affect the ionic transportation in electrolyte. In such case the cell energy densities predicted for Case I and Case III are similar. As the loading increases, both cases predict the energy density to increase before a critical value, above which the energy density starts to decrease. However, for Case I the critical loading is 6 mAh/cm^2, while Case III predicts a lower critical value (4 mAh/cm^2). In addition, Case III predicts a rapid decrease of energy density for loading higher than 5 mAh/cm^2, such that Case I overpredicts the energy density by 110.8% when the cell loading is 7 mAh/cm^2. Such striking difference in model predictions highlights the necessity of incorporating the effect of active material volume change when performing design optimization for cell composed of high-capacity anode.

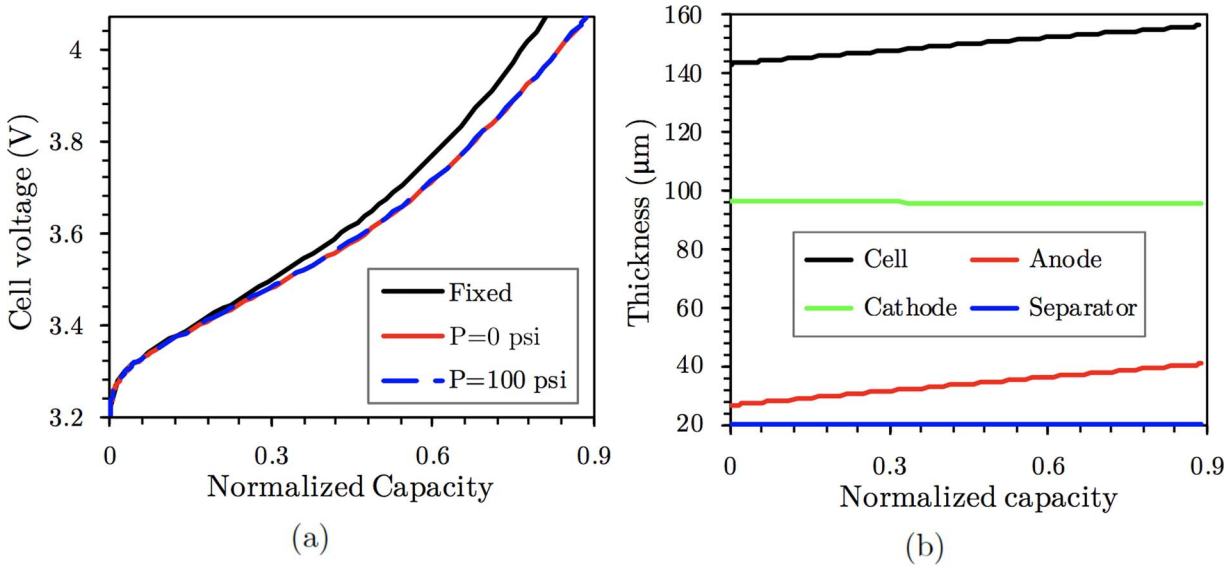

Figure 5. (a) Variation of cell voltage versus the normalized capacity when the cell is charged at 1C; (b) variations of cell thickness and the average porosity of each compoenent versus the normalized capacity when the cell is free to expand (P = 0 psi).

The effect of active material volume change is also affected by the fixture condition of the cell. Figure 5a demonstrates the voltage response of the cell (Case III) when it is either completely constrained in size or allowed to expand/contract under a constant externally applied pressure in the thickness direction. The pressure is applied on the positive current collector, while the negative current collector remains fixed. When the applied pressure P = 0 psi, the cell is free to expand/contract without any limitation in the thickness direction. Compared to the configuration with P = 0 psi, the cell has an additional overpotential of about 104 mV when it is constrained from any dimensional change. This is due to the larger compressive stress and the more notable porosity reduction in this fixture configuration.

While allowing the cell to expand increases the accessible capacity, it also implies more significant volume change of the cell. Figure 5b shows the evolution of the thickness of each component and the entire cell when P = 0 psi. At the end of 1C charge, the thickness of the cell increases from 143.3 μ to 156.3 μm. The volume change of the cell mainly comes from the expansion of the anode, the thickness of which increases from 26.9 μm to 40.9 μm. As $\sigma_{xx} = 0$ MPa when P = 0 psi, the separator only experiences rigid motion without any deformation. As a result, the thickness of the separator does not change during the charging process. The thickness of the cathode is slightly decreased due to the contraction of the NMC particles.

Figures 6a–6c further illustrate the effect of fixture condition on the porosity variation in each component when the cell is charged to 93.1% (maximum for the fixed ends configuration). While predicting similar pattern of porosity distribution, the average porosity in each component is the lowest when both ends of the cell are fixed. This is due to the constrained electrode deformation, which requires the volume change induced by lithium insertion/extraction to go into the empty space (pores), according to Equation 7. Applying a small pressure (P = 100 psi) partially constrains the electrode expansion, so the average porosity in each component is slightly smaller compare to those when P = 0 psi. Finally, Figure 6d shows that distributions of σ_h when the cell is under different fixture conditions. It can be seen that when both ends of the cell are fixed, the hydrostatic stress in the anode will have higher magnitude and nonuniformity, which could lead to accelerated anode degradation especially near the separator. In addition, while a compressive stress of −22 MPa is developed in the cathode when both ends of the cell are fixed, the cathode stress is actually tensile when P = 0 psi due to the contraction of NMC particles as Li is extracted. As the volume change of NMC particles is small, the magnitude of stress is much smaller than the anode stress (about 2 MPa).

Note that when P = 0 psi, $\sigma_{xx} = 0$ MPa and thus σ_h is only determined by the in-plane stress. However, even when the cell is allowed to freely expand in the thickness direction, the magnitude of average σ_h in anode is still larger than 200 MPa. This again highlights the necessity to consider both in-plane and out-of-plane stresses when modeling/designing LIBs with large capacity electrode materials. In addition, while the compressive electrode stress is not expected to cause crack initiation or propagation in Si particles, the compressive stress may already be high enough to cause the damage of the binder of which the compressive strength is around 80 MPa. This would lead to an increase of cell resistance and a decrease of cell capacity due to the loss of connection between the active material and the current collector. Further research is required to determine ways to limit the stress level within the cell, such as limiting the state-of-charge of the cell, utlization of composite anode (Si/C), allowing in-plane displacement, or any reasonable combination of them. The model can also be used to develop requirements for binder properties.

Conclusions

In this work, the Pseudo2D battery model was consistently reformulated based on the finite strain theory to incorporate the coupled effects of large electrochemical-mechanical deformations at both particle and electrode levels. As all governing equations are formulated in the reference (undeformed) geometry, the model was able to approximate the effect of large particle/cell deformations without resorting to remeshing to accommodate the deforming problem domain. We showed that in the proposed model the electrode deformation, porosity variation and the electrochemical processes were consistently coupled. As a result, the model can provide additional information such as the variation of specific surface area, which has not been reported in existing models.

Simulation results showed that there were significant additional overpotentials associated with porosity reduction and compressive hydrostatic stress when the effect of active material volume change was incorporated. The accessible capacity/energy density of the cell were generally overpredicted if particle deformation was assumed negligible, especially at high charge rate, low initial porosity and high cell loading. It was also shown that the porosity variation and stress evolution within the cell were strongly affected by the fixture condition. Therefore, this model can serve as a numerical tool to achieve the

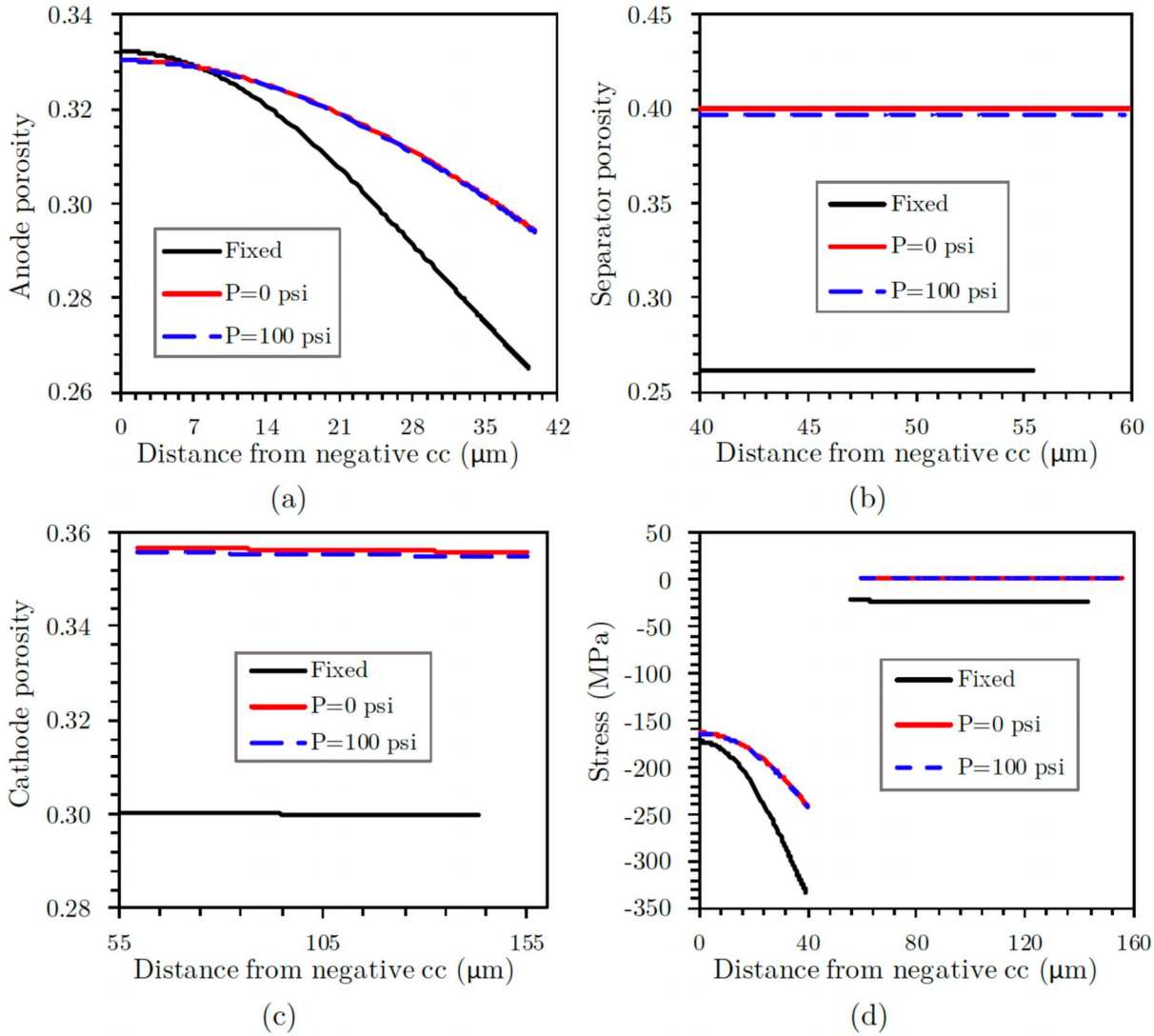

Figure 6. Variation of porosity versus the distance from the negative current collector within (a) anode, (b) separator and (c) cathode. (d) Variation of σ_h in anode and cathode versus the distance from the negative current collector. All cells are charged to 93.1% at 1C.

optimal design of a high-capacity cell in terms of capacity/energy density, allowable stress and allowable volume change. The model also shed light on the potential significance of in-plane stress, which deserves further numerical and experimental investigations.

In the future, the model will be further developed to couple the particle-level diffusion-induced stress with the electrode stress to provide more insight about cell capacity fade due to the fracture of active material. Modeling of Si/C composite anode will also be investigated.

Acknowledgment

This work was authored by Alliance for Sustainable Energy, LLC, the manager and operator of the National Renewable Energy Laboratory for the U.S. Department of Energy (DOE) under Contract No. DE-AC36-08GO28308. Funding was provided by the U.S. DOE Office of Vehicle Technologies Energy Storage Program, program manager Brian Cunningham. The views expressed in the article do not necessarily represent the views of the DOE or the U.S. Government. The U.S. Government retains and the publisher, by accepting the article for publication, acknowledges that the U.S. Government retains a nonexclusive, paid-up, irrevocable, worldwide license to publish or reproduce the published form of this work, or allow others to do so, for U.S. Government purposes.

Appendix A: Explicit Forms of Governing Equations in 1D

Table AI. Explicit forms of the governing equations. Derivatives are defined in the reference configuration.

Variable	Governing equation
c_s	$\frac{\partial}{\partial t}\left[\frac{\varepsilon_s}{\varepsilon_{s,0}}(1+\frac{\partial u}{\partial X})c_s\right] = \frac{1}{R^2}\frac{\partial}{\partial R}\left[R^2 D_E\left[\frac{\varepsilon_s}{\varepsilon_{s,0}}(1+\frac{\partial u}{\partial X})\right]^{1/3}\frac{\partial c_s}{\partial R}\right]$
ε_s	$\frac{\partial}{\partial t}\left[(1+\frac{\partial u}{\partial X})\varepsilon_s\right] = -\frac{s\Omega}{nF}(1+\frac{\partial u}{\partial X})i_E a$
ϕ_s	$\frac{\partial i_s}{\partial X} = -(1+\frac{\partial u}{\partial X})i_E a$
	$i_s = -\kappa_{s,\text{eff}}\nabla\phi_s,\ \kappa_{s,\text{eff}} = \kappa_s\varepsilon_s^b/(1+\frac{\partial u}{\partial X})$
ϕ_e	$\frac{\partial i_e}{\partial X} = (1+\frac{\partial u}{\partial X})i_E a$
	$i_e = -\kappa_{e,\text{eff}}\nabla\phi_e + \left(\frac{2\kappa_{e,\text{eff}}RT}{F}\right)\left(1+\frac{\partial \ln f_\pm}{\partial \ln c_e}\right)(1-t_+)\nabla\ln c_e$
	$\kappa_{e,\text{eff}} = \kappa_e\varepsilon_e^b/(1+\frac{\partial u}{\partial X})$
c_e	$\varepsilon_e(1+\frac{\partial u}{\partial X})\frac{\partial c_e}{\partial t} = \frac{\partial}{\partial X}(D_{e,\text{eff}}\frac{\partial c_e}{\partial X} - \frac{\mathbf{i}_e t_+}{F}) + \frac{s}{nF}(1+\frac{\partial u}{\partial X})i_E a$
	$D_{e,\text{eff}} = D_e\varepsilon_e^b/(1+\frac{\partial u}{\partial X})$
u	$\nabla(\mathbf{FS})_{XX} = 0$
	$(\mathbf{FS})_{XX} = (1+\frac{\partial u}{\partial X})(1+\frac{\Omega\Delta C_{s,\text{avg}}}{3})\frac{E(1-\nu)}{2(1+\nu)(1-2\nu)}$
	$\times\left[\left(\frac{1+\frac{\partial u}{\partial X}}{1+\frac{\Omega\Delta C_{s,\text{avg}}}{3}}\right)^2 + \frac{2\nu}{(1-\nu)(1+\frac{\Omega\Delta C_{s,\text{avg}}}{3})^2} - \frac{1+\nu}{1-\nu}\right]$

Appendix B: Material Properties

Table BI. Expressions for model parameters used in this work. The unit of C_e is kmol/m^3. $T = 303.15\ K$ is temperature and x is the intercalation fraction of the active material. The electrolyte is composed of LiPF6 in EC/EMC (30%:70% by weight).

Property	Expression
E^{eq}_{Si}(V) vs Li^+/Li	$-4.76x^6 + 9.34x^5\ 1.8x^4\ 7.13x^3 + 5.8x^2 - 1.94x + 0.62$
E^{eq}_{NMC}(V) vs Li^+/Li	$5.314735633000300 - 3640.117692001490x^{14} + 13176.57544484270x^{13} - 14557.42062291360x^{12} - 1571.094264365090x^{11} + 12656.30978512400x^{10} - 2057.808873526350x^9 - 10743.74333186190x^8 + 8698.112755348720x^7 - 829.7904604107030x^6 - 2073.765547574810x^5 + 1190.223421193310x^4 - 272.4851668445780x^3 + 27.23409218042130x^2 - 4.158276603609060x - 5.573191762723310 \times 10^{-4} \times \exp(6.560240842659690x^{41.48209275061330})$
D_{Li^+} (m^2/s)	$10^{-4\times(D_0+D_1C_e+D_2C_e^2)}$
	$D_0 = -0.5688226 - 1607.003/(T - Tg)$
	$D_1 = -0.8108721 + 475.2914/(T - Tg)$
	$D_2 = -5.192312 \times 10^{-3} - 33.43827/(T - Tg)$
	$Tg = -24.83763 + 64.07366 \times C_e$
κ_l (S/m)	$K1 \times C_e - K2 \times C_e^2 + K3 \times C_e^3 - K4 \times C_e^4$
	$K1 = 0.0001909446T^2 - 0.08038545T + 9.00341$
	$K2 = -0.00000002887587T^4 + 0.00003483638T^3 - 0.01583677T^2 + 3.195295T - 241.4638$
	$K3 = 0.00000001653786T^4 - 0.0000199876T^3 + 0.009071155T^2 - 1.828064T + 138.0976$
	$K4 = -0.0000000027919 65T^4 + 0.000003377143T^3 - 0.001532707T^2 + 0.3090003T - 23.35671$
$t^+_{Li^+}$	$A \times C_e^2 + B \times C_e + C$
	$A = -0.0000002876102T^2 + 0.0002077407T - 0.03881203$
	$B = 0.000001161463T^2 - 0.00086825T + 0.1777266$
	$C = -0.0000006766258T^2 + 0.0006389189T + 0.3091761$
$\frac{d \ln f_\pm}{d \ln c_l}$	$A \times C_e^2 - B \times C_e - C$
	$A = 0.54 \exp(329.0/T)$
	$B = -0.00225 \exp(1360/T)$
	$C = 0.341 \exp(261.0/T) - 1$
$D_{s,NMC}$ (m^2/s)	3×10^A
	$A = -250.9010843479270x^{10} + 2391.026725259970x^9 - 4868.420267611360x^8 - 83.31104102921070x^7 + 10576.36028329000x^6 - 12683.24548348120x^5 + 5016.272167775530x^4 + 982.4896659649480x^3 - 1502.439339070900x^2 + 472.3709304247700x - 65.26092046397090)$
$i_{0,NMC}$ (A/m^2)	$(16.50452829641290x^5 - 75.23567141488800x^4 + 124.0524690073040x^3 - 94.16571081287610x^2 + 32.49768821737960x - 3.585290065824760) \times (C_e/1.2)^{0.5} \times 10.0$

ORCID

Weijie Mai https://orcid.org/0000-0001-8138-8104
Andrew Colclasure https://orcid.org/0000-0002-9574-5106
Kandler Smith https://orcid.org/0000-0001-7011-0377

References

1. L. Lu, X. Han, J. Li, J. Hua, and M. Ouyang, *J. Power Sources*, **226**, 272 (2013).
2. DOE, US, *US Department of Energy, January*, 31 (2013).
3. W. Zhang, *J. Power Sources*, **196**, 13 (2011).
4. X. Zhang, A. M. Sastry, and W. Shyy, *J. Electrochem. Soc.*, **155**, A542 (2008).
5. Y. T. Cheng and M. W. Verbrugge, *Journal of Power Sources*, **190**, 453 (2009).
6. J. Christensen and J. Newman, *J. Solid State Electrochem.*, **10**, 293 (2006).
7. K. Zhao, M. Pharr, S. Cai, J. J. Vlassak, and Z. Suo, *J. Am. Ceram. Soc.*, **94**, s226 (2011).
8. Z. Cui, F. Gao, and J. Qu, *J. Mech. Phys. Solids*, **60**, 1280 (2012).
9. T. F. Fuller, M. Doyle, and J. Newman, *J. Electrochem. Soc.*, **141**, 1 (1994).
10. M. Doyle, J. Newman, A. S. Gozdz, C. N. Schmutz, and J. M. Tarascon, *J. Electrochem. Soc.*, **143**, 1890 (1996).
11. G. Sikha, B. N. Popov, and R. E. White, *J. Electrochem. Soc.*, **151**, A1104 (2004).
12. M. Jain, G. Nagasubramanian, R. G. Jungst, and J. W. Weidner, *J. Electrochem. Soc.*, **146**, 4023 (1999).
13. P. M. Gomadam and J. W. Weidner, *J. Electrochem. Soc.*, **153**, A179 (2006).
14. T. R. Garrick, X. Huang, V. Srinivasan, and J. W. Weidner, *J. Electrochem. Soc.*, **164**, E3552 (2017).
15. T. R. Garrick, K. Higa, S. Wu, Y, Dai, X. Huang, V. Srinivasan, and J. W. Weidner, *J. Electrochem. Soc.*, **164**, E3592 (2017).
16. A. J. Louli, J. Li, S. Trussler, C. R. Fell, and J. R. Dahn, *J. Electrochem. Soc.*, **164**, A2689 (2017).
17. L. Y. Beaulieu, K. W. Eberman, R. L. Turner, L. J. Krause, and J. R. Dahn, *Electrochem. Solid-State Lett.*, **4**, A137 (2001).
18. B. Wu and W. Lu, *J. Power Sources*, **360**, 360 (2017).
19. J. Kováčik, *J. Mater. Sci. Lett.*, **18**, 1007 (1999).
20. M. Wang and X. Xiao, *J. Power Sources*, **326**, 365 (2016).
21. B. Lu, Y. Song, Q. Zhang, J. Pan, Y. T. Cheng, and J. Zhang, *Phys. Chem. Chem. Phys.*, **18**, 4721 (2016).
22. R. Xu, L. S. de Vasconcelos, and K. Zhao, *J. Mater. Res.*, **31**, 2715 (2016).
23. M. N. Obrovac, L. Christensen, D. B. Le, and J. R. Dahn, *J. Electrochem. Soc.*, **154**, A849 (2007).